Variational Bayesian inversion of synthetic 3D controlled-source electromagnetic geophysical data

Sebastien Penz, Bernard Duchêne, Ali Mohammad-Djafari

GEOPHYSICS, VOL. 83, NO. 1 (JANUARY-FEBRUARY 2018); P. E25–E36, 9 FIGS.
10.1190/GEO2016-0682.1

Variational Bayesian inversion of synthetic 3D controlled-source electromagnetic geophysical data

Sébastien Penz[1], Bernard Duchêne[2], and Ali Mohammad-Djafari[2]

ABSTRACT

Inversion of controlled-source electromagnetic data is dealt with for a geophysical application. The goal is to retrieve a map of conductivity of an unknown body embedded in a layered underground from measurements of the scattered electric field that results from its interaction with a known interrogating wave. This constitutes an inverse scattering problem whose associated forward problem is described by means of electric field domain integral equations. The inverse problem is solved in a Bayesian framework in which prior information is introduced via a Gauss-Markov-Potts model. This model describes the body as being composed of a finite number of different materials distributed into compact homogeneous regions. The posterior distribution of the unknowns is approached by means of the variational Bayesian approximation as a separable distribution that minimizes the Kullback-Leibler divergence with respect to the posterior law. Thus, we get a parametric model for the distributions of the induced currents, the conductivity contrast, and the various parameters of the prior model that are obtained following a semisupervised iterative approach. This method is applied to multifrequency synthetic data corresponding to a 3D crosswell configuration in which the sought body is made of two separated anomalies, a conductive heterogeneity and a resistive one, and its results are compared with that given by the classic contrast source inversion (CSI). The method succeeds in retrieving compact homogeneous regions that correspond to the two anomalies whose shape and conductivities are obtained with a good precision compared with that obtained with CSI.

INTRODUCTION

Geologic storage is one of the solutions investigated at the present time to reduce the release of CO_2 in the atmosphere. In this framework, an experiment is led in the pilot site of Hontomín (Spain), where CO_2 is injected in a deep saline aquifer to be stored (Ogaya et al., 2014). During the injection phase and for a long time after that, monitoring of the storage site is necessary to make sure that CO_2 remains at the intended place and to detect possible leakages toward the surface. Among the various monitoring methods, controlled-source electromagnetic (CSEM) techniques are good candidates due to their noninvasive nature, their low cost, and their sensitivity to the electrical conductivity of the media and, hence, to the CO_2 saturation of the latter. So, this is the application considered herein. The goal is to monitor the evolution of a CO_2 plume stored in a deep layer of a known stratified underground by means of sources (herein electric dipoles) and receivers disposed on the ground or in boreholes, several of which preexist in the Hontomín site around the storage location. It is worth noting that, at the present time, the quantity of CO_2 injected in the storage site is not sufficient to collect significative field data so that this study is led on a synthetic experiment inspired from the Hontomín site but with a very simplified configuration. However, the layered underground model (taken from Ogaya et al., 2014) is realistic, as well as the conductivity contrast and the dimensions of the body.

Manuscript received by the Editor 14 December 2016; revised manuscript received 7 June 2017; published ahead of production 12 October 2017; published online 01 December 2017.
[1]Formerly Laboratoire des Signaux et Systèmes, Gif-sur-Yvette, France; presently Bureau de Recherches Géologiques et Minières (BRGM), DRP/RAI, Orléans, France. E-mail: s.penz@brgm.fr.
[2]Laboratoire des Signaux et Systèmes (UMR8506: CNRS — CentraleSupélec — Univ Paris-Sud 11), Gif-sur-Yvette, France. E-mail: bernard.duchene@l2s.centralesupelec.fr.

DOI:10.1190/geo2016-0682.1

The problem at hand is turned into that of retrieving an image that consists of a map of the electrical conductivity (or resistivity) of an unknown body embedded in a layered underground from measurements of the scattered electric field that results from its interaction with a known interrogating wave. This constitutes a nonlinear inverse scattering problem, in which "inverse" denotes opposition to the forward problem that would consist of computing the scattered electric field when the underground, the body, and the interrogating wave are known.

The development of imaging solutions able to provide reliable 3D images of underground features is of considerable interest for exploration geophysics or monitoring purposes. Hence, since the early 1990s, there was an important effort in the geologic field to develop electromagnetic prospection tools and related inversion algorithms. The first approaches were fast imaging methods such as migration by analytic continuation (Zhdanov et al., 1996; Hokstad and Røsten, 2007) and linearization techniques based on the Born or Rytov approximations (Habashi et al., 1993; Zhdanov and Fang, 1996). These techniques only provide low-resolution images whose quality is not sufficient for retrieving the subsurface conductivity structures, and linearized solutions do not work when the body shows a high conductivity contrast with respect to the underground. More rigorous methods were proposed to deal with the nonlinearity of the problem. Most of these methods belong to the deterministic inversion framework and turn the problem into an optimization one, in which the goal is to minimize a cost functional that expresses the discrepancy between the scattered field data and the output of the forward model (Abubakar and van den Berg, 1998; Constable and Weiss, 2006; Gribenko and Zhdanov, 2007; Plessix and Mulder, 2008; Commer and Newman, 2009; Wiik et al., 2011; Egbert and Kelbert, 2012). However, in addition to being nonlinear, inverse scattering problems are known to be also ill-posed, which means that they need to be regularized to ensure the uniqueness and stability of the solution. This regularization usually consists of introducing a priori information on the sought solution and, with the above-mentioned deterministic approaches, this information is added in the cost functional through a regularization term (Tikhonov, 1963; Portniaguine and Zhdanov, 1999), which is more or less easy, depending upon the prior that must be accounted for.

To overcome the limitations of deterministic methods and, in particular, to account for uncertainties, researchers turned to stochastic inversion methods such as simulated annealing (Roth and Zach, 2007) and genetic algorithms (Hunziker et al., 2014), keeping with geophysical applications. However, these methods are usually avoided because they are wildly heuristic and there is no proven optimal strategy for tuning them to a given problem (Mosegaard and Sambridge, 2002). More tractable methods have been developed in the Bayesian framework (Tarantola and Valette, 1982) and applied to CSEM data inversion (Chen et al., 2007; Gunning et al., 2010; Minsley, 2011; Trainor-Guitton and Hoversten, 2011; Buland and Kolbjørnsen, 2012; Ray and Key, 2012; Ray et al., 2014; Gehrmann et al., 2015). These methods take into account uncertainties (modeling errors and measurement noises) through an appropriate likelihood function and allow us to introduce in an easy way all the prior information we may have on the unknowns through prior probability distributions. The product of prior distributions and likelihood then yields a joint posterior probability law of all the unknowns.

Once the posterior law is expressed, a usual way is to implement a Markov Chain Monte Carlo method (MCMC) (Robert and Casella, 2000) that estimates the posterior distribution through a stochastic sampling method such as a Metropolis-Hastings or a transdimensional Metropolis-Hastings-Green algorithm (Minsley, 2011; Trainor-Guitton and Hoversten, 2011; Buland and Kolbjørnsen, 2012; Ray and Key, 2012; Ray et al., 2014; Gehrmann et al., 2015), a slice sampling method (Chen et al., 2007; Trainor-Guitton and Hoversten, 2011), or a Gibbs sampler (Rothman, 1986; Sen and Stoffa, 1996). However, these methods are particularly costly in terms of computations because they require drawing a significant number of samples. They are, therefore, hardly applicable to large-scale problems such as the inversion of 3D CSEM data, and the state of the art only mentions 1D configurations (Ray and Key, 2012) or 2D configurations (Ray et al., 2014) with a 1D forward approximation. This is the reason why we introduce, herein, the variational Bayesian approximation (VBA) as an alternative to MCMC methods for CSEM Bayesian inversion. The purpose of this approach is to approximate the posterior distribution by a separable law. Calculations are performed analytically, which reduce significantly the computation cost and, thus, allows us to handle problems of much higher dimensions than with MCMC methods. The VBA method has already been applied with success to 2D inversion problems in other domains with different configurations, i.e., monofrequency optical diffraction tomography in stratified media (Ayasso et al., 2012) and multifrequency microwave imaging in homogeneous backgrounds (Gharsalli et al., 2014). The originality herein is that it is applied to a 3D inversion problem for a geophysical application in which multifrequency data and stratified underground are considered.

This paper is organized as follows. "The forward model" section presents the forward model based on frequency-domain electric field volume integral equations and its numerical solution based on discrete counterparts of the above-mentioned equations obtained by means of the method of moments. The "Deterministic inversion" section presents a deterministic inversion method, i.e., contrast source inversion (CSI), which will serve as a reference to evaluate the performance of VBA. The Bayesian inversion approach is addressed in the "Bayesian inversion approach" section, which displays, in particular, the prior and posterior probability laws. It is worth noting that the former account for the prior information that we would like to introduce in the inversion algorithm which consists of the fact that CO_2 is supposed to remain confined in a few compact domains with homogeneous conductivity distributions corresponding to homogeneous CO_2 saturations (Bourgeois and Girard, 2010) located in the intended storage layer or, possibly, in case of leakage of CO_2 toward an upper aquifer layer, in several such domains with different conductivity distributions. This prior knowledge is translated by a Gauss-Markov-Potts model (Mohammad-Djafari, 2008) that describes the conductivity distribution as a Gaussian mixture, where each Gaussian law corresponds to a given conductivity distribution, and that accounts for the compactness of the domains by means of a hidden Potts-Markov field. The "Bayesian computations" section presents the VBA, and it details, in particular, the parameters of the distributions involved in the approximate joint posterior law. The "Application and results" section displays the results obtained by means of VBA on a very simple synthetic experiment as a proof of concept of its applicability to the application considered herein. The body then consists of two heterogeneities, one being conductive and the other resistive, and it is probed at six different frequencies from sources and receivers located in four boreholes surrounding the test domain that is sup-

posed to contain the body. Finally, the last section highlights the advantages of VBA and opens some prospects.

THE FORWARD MODEL

Frequency-domain electric field integral equations

Let us consider a 3D body Ω supposed to be contained in a test domain $\mathcal{D}$ embedded in the layer l of a 1D stratified underground made of N_l nonmagnetic homogeneous layers of various thicknesses. The body is illuminated by a time harmonic electromagnetic wave of which implicit time dependence is chosen as $\exp(-i\omega t)$ and of which frequency is low enough to consider that the displacement currents are negligible, so that the body and the different layers are characterized by their respective conductivities σ_Ω and σ_l ($l = 1, 2, \ldots, N_l$) or, equivalently, by their resistivities ρ_Ω and ρ_l. Let us now define in $\mathcal{D}$ a normalized contrast function χ that expresses the contrast of conductivity between the body Ω and the embedding layer l:

$$\chi(\mathbf{r}) = \frac{\sigma(\mathbf{r}) - \sigma_l}{\sigma_l}, \quad \mathbf{r} \in \mathcal{D}. \tag{1}$$

In the presence of an electric field $\mathbf{E}$, this conductivity contrast induces fictitious Huygens type sources $\mathbf{w}$ (or contrast sources), $\mathbf{w}(\mathbf{r}) = \chi(\mathbf{r})\mathbf{E}(\mathbf{r})$, which are in fact a distribution of conduction currents defined in $\mathcal{D}$ and null outside the body.

By applying Green's theorem to the Helmholtz wave equations satisfied by the fields and by accounting for continuity and radiation conditions (Colton and Kress, 1992; Chew, 1995), we get two coupled integral equations, the first one of which, denoted as the *coupling* or *state equation*, links the unknown total electric field $\mathbf{E}$ in $\mathcal{D}$ to the induced sources $\mathbf{w}$:

$$\mathbf{E}(\mathbf{r}) = \mathbf{E}^{\text{inc}}(\mathbf{r}) + i\omega\mu_0\sigma_l \int_{\mathcal{D}} \bar{\mathbf{G}}_e(\mathbf{r}, \mathbf{r}')\mathbf{w}(\mathbf{r}')d\mathbf{r}', \quad \mathbf{r} \in \mathcal{D}, \tag{2}$$

where ω is the angular frequency, μ_0 is the magnetic permeability of the vacuum, and $\mathbf{E}^{\text{inc}}(\mathbf{r})$ and $\bar{\mathbf{G}}_e(\mathbf{r}, \mathbf{r}')$ are the so-called incident field and the electric dyadic Green's function (Wannamaker et al., 1984) that represent, respectively, the primary electric field due to the interrogating source and the field due to a point source located at $\mathbf{r}'$, both observed at $\mathbf{r}$ in the layered underground in the absence of the body. It is worth noting that the unknown total field $\mathbf{E}$ within the body appears on both sides of the above equation, hidden in the sources $\mathbf{w}$ on the right side. This allows one to get two versions of this equation, i.e., a field formulation (used, e.g., in Kleinman and van den Berg, 1992) in which the sources $\mathbf{w}(\mathbf{r}')$ are explicitly replaced by the product $\chi(\mathbf{r}')\mathbf{E}(\mathbf{r}')$ or a source-type integral equation (used, e.g., in van den Berg and Kleinman [1997] and adopted herein from now on) obtained by multiplying both sides of equation 2 by $\chi(\mathbf{r})$.

The second equation, denoted as the *observation* or *data equation*, expresses the so-called scattered field $\mathbf{E}^{\text{sc}}$ (i.e., the secondary field due to the presence of the body), measured on an observation domain $\mathcal{S}$ anywhere outside $\mathcal{D}$, as radiated by the induced sources $\mathbf{w}$:

$$\mathbf{E}^{\text{sc}}(\mathbf{r}) = i\omega\mu_0\sigma_l \int_{\mathcal{D}} \bar{\mathbf{G}}_e(\mathbf{r}, \mathbf{r}')\mathbf{w}(\mathbf{r}')d\mathbf{r}', \mathbf{r} \in \mathcal{S}. \tag{3}$$

Numerical solution

Assuming that $\mathbf{E}^{\text{inc}}$ and χ are known, the forward problem consists of, first, solving equation 2 (in its source-type form) for $\mathbf{w}$ and, then, equation 3 for $\mathbf{E}^{\text{sc}}$. This is done from discrete counterparts of these equations obtained by means of the *method of moments* (MoM) with pulse basis functions and point matching (Newman et al., 1986; Newman and Hohmann, 1988). The test domain is then subdivided into $N_D = N_x \times N_y \times N_z$ parallelepipedic elementary cells over which $\mathbf{E}$ and χ are considered as constant. In the last equation, N_x, N_y, and N_z are the number of cells along the corresponding spatial axes. In an operator notation, this leads to the two following linear systems:

$$\mathbf{w}(\mathbf{r}_i) = \chi(\mathbf{r}_i)\mathbf{E}^{\text{inc}}(\mathbf{r}_i) + \chi(\mathbf{r}_i)\sum_{j=1}^{N_D} \bar{\mathbf{G}}^c(\mathbf{r}_i, \mathbf{r}_j)\mathbf{w}(\mathbf{r}_j), \quad i = 1, \ldots, N_D, \tag{4}$$

$$\mathbf{E}^{\text{sc}}(\mathbf{r}_i) = \sum_{j=1}^{N_D} \bar{\mathbf{G}}^o(\mathbf{r}_i, \mathbf{r}_j)\mathbf{w}(\mathbf{r}_j), \quad i = 1, \ldots, N_S, \tag{5}$$

where N_S is the number of observation points and the elements of the tensors $\bar{\mathbf{G}}^c$ and $\bar{\mathbf{G}}^o$ result from the integration of the dyadic Green's function over the elementary cells. Although the choice of pulse basis functions is not optimal because it does not ensure the continuity of the normal component of the electric flux density at the interface between two neighboring elementary cells, it has the advantage of preserving the convolutional nature of equations 2 and 3, which is important as will be seen later. Furthermore, this formulation is expected to be accurate enough as far as we are concerned with bodies whose contrasts are not too high and that are illuminated at a low frequency. Let us now rewrite the above tensorial equations in a matrix form by appending quantities corresponding to the three spatial components. It is worth noting that matrix $\mathbf{G}^{\mathbf{c}}$, which corresponds to the tensor $\bar{\mathbf{G}}^c$ of equation 4, is a block-Toeplitz matrix (Gao, 2005; Goreinov et al., 2009). The redundancy of its terms allows us to reduce its storage size from $3N_D \times 3N_D$ to $(2N_x - 1) \times (2N_y - 1) \times N_z^2$. Furthermore, a huge amount of computation time can be saved by performing the convolution products that appear in equations 2 and 3 in the spectral domain (i.e., in the k-space) where they are reduced to matrix-vector products (Lesselier and Duchêne, 1991; Gao, 2005); hence, equation 4 is solved in this way by means of the *bi-conjugate gradient stabilized-fast Fourier transform method* (BCGS-FFT) (Xu and Liu, 2002).

DETERMINISTIC INVERSION

Problem statement

Let us now consider the inverse problem that consists of retrieving the unknown contrast function χ within the test domain $\mathcal{D}$ from measurements of the scattered electric field at N_S points in the measurement domain $\mathcal{S}$. With iterative deterministic approaches, this inverse problem is turned into an optimization problem where χ is sought by minimizing a cost functional that expresses the misfit between the data (the scattered field) and the direct model output, in other words, the error in satisfying the observation equation. However, in addition to being nonlinear, inverse scattering problems are also known to be ill-posed, which means that they need to be regularized. This can be done in the sense of Tikhonov (Tikhonov, 1963), for example, where a pri-

DOI:10.1190/geo2016-0682.1

ori information on the sought solution is introduced in the functional to be minimized. Hence, this functional will likely take the form

$$\mathcal{J}(\boldsymbol{\chi}) = \|\mathbf{E}^{\text{sc}} - \mathcal{F}(\boldsymbol{\chi})\|_{\mathcal{S}}^2 + \lambda\|\mathcal{R}(\boldsymbol{\chi})\|_{\mathcal{D}}^2, \tag{6}$$

where $\boldsymbol{\chi}$ is the conductivity contrast model, $\mathcal{F}$ is the forward operator, $\mathcal{R}$ is the regularization operator, $\|.\|_A$ represents the norm associated to the inner product $\langle .,. \rangle_A$ in $L^2(A)$, with $A = \mathcal{S}$ or $\mathcal{D}$, and $\lambda > 0$ is a regularization parameter that expresses the relative confidence that we can have in the data and in the a priori. As for the regularization term, it can express the fact that a minimum norm solution is sought, which would lead to smoothed solutions, or, on the contrary, it can be built up to preserve the edges (Charbonnier et al., 1997) (it should be noted that in that case, it is not quadratic), or it can account for the coupling equation as in the modified gradient method (Kleinman and van den Berg, 1992) and so on. Let us here emphasize the fact that the prior information that the sought body is made of compact homogeneous regions, i.e., the prior information that we would like to account for herein, has already been introduced in some deterministic inversion methods by considering regularization operators that involve low-dimensional parametrizations of the unknown body that is then sought with a shape- (Miller et al., 2000) or model-based (Abubakar et al., 2009) approach or through a level set representation (Dorn et al., 2000).

As for the minimization problem that aims at finding the parameter distribution that minimizes $\mathcal{J}(\boldsymbol{\chi})$, numerous methods have been proposed to solve it. To focus on the electromagnetic case for geophysical applications, let us quote the Gauss-Newton approaches of Constable and Weiss (2006), Abubakar et al. (2006), and Li et al. (2011) that consider 1D, 2D, and 3D inversion problems, respectively, those of Commer and Newman (2009) and Gribenko and Zhdanov (2007) that solve the 3D problem by means of a nonlinear conjugate gradient method, and, finally, those of Plessix and Mulder (2008) that use a quasi-Newton method associated with depth weighting to limit memory consumption and improve the convergence rate of the method. Some other methods use a decomposition of the forward problem into bilinear (the Born iterative method [Li et al., 2004] and contrast-source inversion) or trilinear problems (Barrière et al., 2007) involving χ, $\mathbf{w}$, and/or $\mathbf{E}$.

The CSI method

The CSI method, first introduced by van den Berg and Kleinman (1997), uses the same formulation of the forward problem as in previous section with coupling and observation equations expressed in terms of conductivity contrast $\boldsymbol{\chi}$ and induced sources (or contrast sources) $\mathbf{w}$. The contrast and the induced sources are sought by minimizing a cost functional $\mathcal{J}(\mathbf{w}, \boldsymbol{\chi})$ consisting of two terms that represent the errors $\mathcal{J}_o(\mathbf{w})$ and $\mathcal{J}_c(\mathbf{w}, \boldsymbol{\chi})$ in satisfying the observation and coupling equations, respectively:

$$\mathcal{J}(\mathbf{w}, \boldsymbol{\chi}) = \mathcal{J}_o(\mathbf{w}) + \mathcal{J}_c(\mathbf{w}, \boldsymbol{\chi}), \tag{7}$$

with

$$\mathcal{J}_o(\mathbf{w}) = \frac{\sum_\nu \|\mathbf{E}_\nu^{\text{sc}} - \mathbf{G}^o \mathbf{w}_\nu\|_{\mathcal{S}}^2}{\sum_\nu \|\mathbf{E}_\nu^{\text{sc}}\|_{\mathcal{S}}^2} \tag{8}$$

and

$$\mathcal{J}_c(\mathbf{w}, \boldsymbol{\chi}) = \frac{\sum_\nu \|\boldsymbol{\chi}\mathbf{E}_\nu^{\text{inc}} - \mathbf{w}_\nu + \boldsymbol{\chi}G^c\mathbf{w}_\nu\|_{\mathcal{D}}^2}{\sum_\nu \|\boldsymbol{\chi}\mathbf{E}_\nu^{\text{inc}}\|_{\mathcal{D}}^2} = \frac{\sum_\nu \|\boldsymbol{\chi}\mathbf{E}_\nu - \mathbf{w}_\nu\|_{\mathcal{D}}^2}{\sum_\nu \|\boldsymbol{\chi}\mathbf{E}_\nu^{\text{inc}}\|_{\mathcal{D}}^2}, \tag{9}$$

where the observation and coupling errors are normalized in such a way that they are equal to one when the contrast sources vanish. In the above equations, the subscript ν stands for the source position, a single frequency being considered. It can be noted that the performances of CSI can be significantly improved by accounting for additional multiplicative or additive constraints in the cost functional, such as a positivity constraint on $\boldsymbol{\sigma}$ (van den Berg and Kleinman, 1997), a total variation term (Abubakar and van den Berg, 2002), or a weighted L_2-norm regularizer (Li et al., 2011), but this falls beyond the scope of this paper because CSI is considered, herein, as a reference solution and we do not aim at performing an exhaustive comparison of CSI solutions with additional constraints against VBA.

The CSI method minimizes the cost functional given by equation 7 in an iterative way by alternately updating the contrast sources and the conductivity contrast with a Polak-Ribière conjugate gradient scheme. Details of the minimization and derivation of the contrast-source and contrast updates are given in van den Berg and Kleinman (1997), Abubakar and van den Berg (1998, 2000), Abubakar (2000), and van den Berg and Abubakar (2001).

Although the cost functionals given by equations 8 and 9 are written for a single frequency, CSI can obviously handle multifrequency data, and this can be done in several ways, from a basic frequency hopping scheme to a simultaneous inversion of data corresponding to several frequencies and, in the latter case, by considering an additive cost functional (the subscript ν of equations 8 and 9 is then replaced by a subscript n that holds for the source position and frequency) as in the original version of the method or a multiplicative one (Abubakar, 2000) as considered herein. This multiplicative cost functional reads

$$\mathcal{C}(\mathbf{w}, \boldsymbol{\chi}) = \prod_f \mathcal{J}_f(\mathbf{w}_f, \boldsymbol{\chi}), \tag{10}$$

where $\mathcal{J}_f$ is the cost for a single frequency f, as described in equation 7.

BAYESIAN INVERSION APPROACH

First, let us define two vectors $\boldsymbol{\epsilon}$ and $\boldsymbol{\xi}$ that represent the measurement uncertainties and all the model errors (due to approximations and discretization issues), respectively. By accounting for these errors, the discrete forward model can be rewritten in a matrix operator notation as follows:

$$\begin{aligned} \mathbf{E}_n^{\text{sc}} &= \mathbf{G}_f^o \mathbf{w}_n + \boldsymbol{\epsilon}_n, \\ \mathbf{w}_n &= \boldsymbol{\chi}\mathbf{E}_n^{\text{inc}} + \boldsymbol{\chi}\mathbf{G}_f^c \mathbf{w}_n + \boldsymbol{\xi}_n. \end{aligned} \tag{11}$$

The subscript n accounts for the different frequencies f and source positions ν; for the sake of clarity, it will be omitted from now on.

In any statistical method, the first step is to characterize $\boldsymbol{\epsilon}$ and $\boldsymbol{\xi}$ and, in the Bayesian approach, probability distributions must be assigned to them. Preliminary studies (Vilamajó et al., 2015) con-

ducted on the Hontomín site have shown that, to a large extent, the experimental uncertainties in the range of 0.5–384 Hz follow Gaussian distributions, so that we can reasonably assume that the observation noise $\boldsymbol{\epsilon}$ follows a centered Gaussian distribution with a fixed variance γ_ϵ^2. As for the coupling noise $\boldsymbol{\xi}$, we have obviously no information about it except for the finiteness of its variance. Although there is absolutely no reason why it should follow such a law, we shall assume that $\boldsymbol{\xi}$ also satisfies a centered Gaussian distribution with fixed variance γ_ξ^2. Indeed, any other choice would lead to a much more complex likelihood term. Elsewhere, this choice is the less informative a priori that can be assigned, and it can be interpreted at a maximum entropy point of view. Furthermore, as will be seen later on, inverse-gamma laws are assigned to γ_ϵ^2 and γ_ξ^2 that are estimated from the data, and this can be interpreted as if $\boldsymbol{\epsilon}$ and $\boldsymbol{\xi}$ were assigned to follow Student's t probability distributions. Such distributions have heavier tails and, hence, yield more robustness against deviation from prior settings than the Gaussian ones (Wang et al., 2016).

From the above observation and coupling equations, we can then write the two following probability laws:

$$p(\mathbf{E}^{\text{sc}}|\mathbf{w}) = \left(\frac{1}{2\pi\gamma_\epsilon^2}\right)^{\frac{N_S}{2}} \exp\left(-\frac{\|\mathbf{E}^{\text{sc}} - \mathbf{G}^o\mathbf{w}\|_{\mathcal{S}}^2}{2\gamma_\epsilon^2}\right), \quad (12)$$

$$p(\mathbf{w}|\boldsymbol{\chi}) = \left(\frac{1}{2\pi\gamma_\xi^2}\right)^{\frac{N_D}{2}} \exp\left(\frac{\|\mathbf{w} - \boldsymbol{\chi}\mathbf{E}^{\text{inc}} - \boldsymbol{\chi}\mathbf{G}^c\mathbf{w}\|_{\mathcal{D}}^2}{2\gamma_\xi^2}\right), \quad (13)$$

where N_D and N_S are the number of cells partitioning the test domain and the number of observation points, respectively.

The prior modeling

A significant advantage of Bayesian inversion methods over deterministic ones is the easiness of introducing *a priori information* in the inversion process. Here, we would like to take into account the fact that the unknown body is composed of a finite number N_k of materials (with different conductivities), and that these materials are distributed in compact homogeneous regions. It can be noted that, herein, "homogeneous" does not mean that the contrast takes a constant value throughout the whole region, but that its values vary slightly around a mean value m_k. This prior information is introduced by means of a hidden field $h(\mathbf{r})$ associated to each cell $\mathbf{r}$. This field can take discrete values k ($k = 1, \ldots, N_k$) which define different classes of materials. These classes are characterized by a contrast that satisfies a Gaussian distribution with mean value m_k and variance γ_k^2:

$$p(\boldsymbol{\chi}(\mathbf{r})|h(\mathbf{r}) = k) = \mathcal{N}(m_k, \gamma_k^2), \quad k = 1, \ldots, N_k. \quad (14)$$

Information relative to the compactness and homogeneity of the different regions is introduced by means of a Potts-Markov model on $\mathbf{h} = \{h(\mathbf{r}), \mathbf{r} \in \mathcal{D}\}$ that expresses the spatial dependence between neighboring cells:

$$p(\mathbf{h}) = \frac{1}{T(\Upsilon)} \exp\left\{\Upsilon \sum_{\mathbf{r}\in\mathcal{D}} \sum_{\mathbf{r}'\in\mathcal{V}_r} \delta[h(\mathbf{r}) - h(\mathbf{r}')]\right\}, \quad (15)$$

where $T(\Upsilon)$ is a normalization factor, Υ determines the degree of dependency between neighbor values, $\mathcal{V}_r$ is the neighborhood of $\mathbf{r}$ (herein made of the six nearest cells), and δ is the Dirac distribution.

The construction of the above model is illustrated in Figure 1 which depicts a configuration in which the sought body is made of two different materials distributed in three compact regions, so that there are $N_k = 3$ classes characterized by respective hidden field values $h(\mathbf{r}) = 1$, 2, or 3 ($h(\mathbf{r}) = 1$ stands for the embedding layer medium) and by contrast values that satisfy Gaussian laws $p(\chi(\mathbf{r})|h(\mathbf{r}) = k) = \mathcal{N}(m_k, \gamma_k^2)$, $k = 1$, 2, or 3.

From now on, the variables γ_ϵ^2, γ_ξ^2, m_k, and γ_k^2, which appear in the above-defined probability distributions, will be denoted as hyperparameters and gathered in a vector $\boldsymbol{\psi}$ ($\boldsymbol{\psi} = \{\gamma_\epsilon^2, \gamma_\xi^2, (m_k, \gamma_k^2, k = 1, \ldots, N_k)\}$). As, in practice, they are not known, these hyperparameters need to be estimated, and, so, prior probability distributions are assigned to them. Concerning the hyperparameters, it has been observed that the reconstruction results are less sensitive to their priors than to that of the parameters. Therefore, to make the computations easier, conjugate prior laws (Bernardo and Smith, 2008) are assigned to the hyperparameters as, in this way, the corresponding posteriors stay in the same distribution family. Hence, their prior distributions read

$$p(m_k) = \mathcal{N}(m_k|\mu_0, \tau_0),\ p(\gamma_k^2) = \mathcal{IG}(\gamma_k^2|\eta_0, \phi_0),$$
$$p(\gamma_\epsilon^2) = \mathcal{IG}(\gamma_\epsilon^2|\eta_{\epsilon 0}, \phi_{\epsilon 0}),\ p(\gamma_\xi^2) = \mathcal{IG}(\gamma_\xi^2|\eta_{\xi 0}, \phi_{\xi 0}), \quad (16)$$

where $\mathcal{IG}$ and $\mathcal{N}$ stand for inverse-gamma and Gaussian distributions, respectively:

$$\mathcal{IG}(\gamma^2|\eta, \phi) \propto (1/\gamma^2)^{\eta-1} \exp(-\phi/\gamma^2),$$
$$\mathcal{N}(m|\mu, \tau) \propto \exp(-(m-\mu)^2/2\tau), \quad (17)$$

and μ_0, τ_0, η_0, ϕ_0, $\eta_{\epsilon 0}$, $\phi_{\epsilon 0}$, $\eta_{\xi 0}$, and $\phi_{\xi 0}$ are meta-hyperparameters that are set to introduce almost noninformative flat prior distributions, i.e., μ_0, η_0, $\eta_{\epsilon 0}$, and $\eta_{\xi 0}$ are set to one, whereas τ_0 is set at a rather high value and ϕ_0, $\phi_{\epsilon 0}$, and $\phi_{\xi 0}$ at low values.

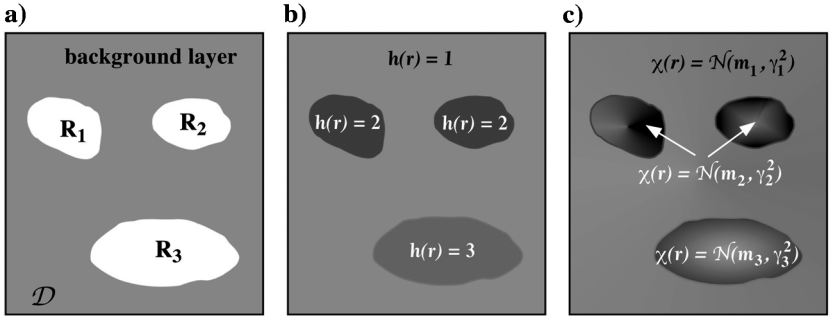

Figure 1. The case of a body made of two different materials distributed in three compact regions: (a) the three regions R_1, R_2, and R_3 (R_1 and R_2 are made of the same material), (b) the hidden field $h(\mathbf{r})$ that can take three different values, and (c) the contrast $\chi(\mathbf{r})$ that is sought as a Gaussian mixture.

Posterior laws

We consider herein a semisupervised inversion process (because the number of classes N_k is supposed to be known) where the contrast $\boldsymbol{\chi}$, the induced currents $\mathbf{w}$, the segmentation $\mathbf{h}$ and the hyperparameters $\boldsymbol{\psi}$ are estimated simultaneously. Using the Bayes rule, the expression of the joint posterior distribution of all the unknowns reads

$$p(\boldsymbol{\chi},\mathbf{w},\mathbf{h},\boldsymbol{\psi}|\mathbf{E}^{sc}) \propto p(\mathbf{E}^{sc}|\mathbf{w},\boldsymbol{\psi})p(\mathbf{w}|\boldsymbol{\chi},\boldsymbol{\psi})p(\boldsymbol{\chi}|\mathbf{h},\boldsymbol{\psi})p(\mathbf{h})p(\boldsymbol{\psi}). \tag{18}$$

The different components of $p(\boldsymbol{\psi})$ are given by equations 16 and 17, whereas the probability laws $p(\boldsymbol{\chi}|\mathbf{h},\boldsymbol{\psi})$ and $p(\mathbf{h})$ are given by equations 14 and 15 and, finally, $p(\mathbf{E}^{sc}|\mathbf{w},\boldsymbol{\psi})$ and $p(\mathbf{w}|\boldsymbol{\chi},\boldsymbol{\psi})$ are given by equations 12 and 13, respectively.

BAYESIAN COMPUTATIONS

VBA

Because all the right-side terms of equation 18 are known, we have the expression of the joint posterior law of all the unknowns (the left-side expression) up to a normalizing factor. From now on, using this expression, different inferences can be done on all the unknowns of the problem. It can be noted, however, that working directly with probability distributions is often not easy. This is the reason why different point estimators, such as the maximum a posteriori (MAP) or the posterior mean (PM), are usually computed. But computations of these estimators are generally also difficult because they require a nonconvex optimization or a hardly tractable integration, respectively. Hence, approximate solution methods, such as the joint maximum a posteriori (JMAP), MCMC, or VBA algorithms, are often used. Concerning JMAP, its main interest is its link with deterministic regularization methods. However, this estimator does not account for all the uncertainties: Particularly, when looking simultaneously to several parameters in an iterative way, at each iteration, each parameter is estimated by considering that the others are certain. As for the MCMC methods, they try, in general, to explore the whole space of the unknowns by generating samples from the joint posterior law. Because they are based upon stochastic samplers whose convergence requires the drawing of a huge number of samples, they are computationally ineffective for high dimensional problems such as those encountered in the inversion of 3D CSEM data, although recent methods allow hastening their convergence (Ray et al., 2013).

The VBA avoids these difficulties by performing an analytical approximation of the posterior law. In return, because VBA does not browse the whole solution space, one could be faced with a drawback of the method: Although a priori information has been introduced in the prior modeling, this may not be sufficient to avoid VBA to be stuck in a local minimum corresponding to a suboptimal solution because the posterior marginal law for the contrast $\boldsymbol{\chi}$ may be multimodal (Gunning et al., 2010; Ray et al., 2013). One possible way to cope with this situation would be to restart the algorithm with different priors.

The idea behind VBA is to approximate the true posterior $p(\mathbf{w},\boldsymbol{\chi},\mathbf{h},\boldsymbol{\psi}|\mathbf{E}^{sc})$ with a separable distribution $q(\mathbf{w},\boldsymbol{\chi},\mathbf{h},\boldsymbol{\psi})$ that minimizes the Kullback-Leibler divergence $\mathrm{KL}(q\|p) = \int q\log(q/p)$ (Kullback and Leibler, 1951; Hinton and van Camp, 1993; Šmídl and Quinn, 2006; Mohammad-Djafari, 2015). Let us first define the separable form as

$$q(\mathbf{w},\boldsymbol{\chi},\mathbf{h},\boldsymbol{\psi}) = \prod_n\prod_{\mathbf{r}} q(w_n(\mathbf{r}))\prod_n q(\gamma^2_{\epsilon_n})q(\gamma^2_{\xi_n}) \times \prod_{\mathbf{r}} q(\chi(\mathbf{r}))\prod_k q(h_k)q(m_k)q(\gamma^2_k), \tag{19}$$

where subscript n stands for the frequency and the source position, subscript k stands for the material class, and $\mathbf{r}$ stands for the cell. The optimal form of q that minimizes the Kullback-Leibler divergence leads to the following parametric distributions (Ayasso, 2010):

$$\begin{aligned}
&q(w_n(\mathbf{r})) = \mathcal{N}(w_n(\mathbf{r})|\tilde{m}_{w_n(\mathbf{r})},\tilde{v}_{w_n(\mathbf{r})}),\\
&q(\chi(\mathbf{r})) = \mathcal{N}(\chi(\mathbf{r})|\tilde{m}_{\chi(\mathbf{r})},\tilde{v}_{\chi(\mathbf{r})}), \quad q(h_k) = \prod_{\mathbf{r}}\tilde{\zeta}_k(\mathbf{r}),\\
&q(m_k) = \mathcal{N}(m_k|\tilde{\mu}_k,\tilde{\tau}_k), \quad q(\gamma^2_k) = \mathcal{IG}(\gamma^2_k|\tilde{\eta}_k,\tilde{\phi}_k),\\
&q(\gamma^2_{\epsilon_n}) = \mathcal{IG}(\gamma^2_{\epsilon_n}|\tilde{\eta}_{\epsilon_n},\tilde{\phi}_{\epsilon_n}), \quad q(\gamma^2_{\xi_n}) = \mathcal{IG}(\gamma^2_{\xi_n}|\tilde{\eta}_{\xi_n},\tilde{\phi}_{\xi_n}),
\end{aligned}$$

where $\tilde{v}$ stands for the variance and $\tilde{\zeta}_k(\mathbf{r})$ is defined by equation 25.

It is worth noting that the tilded parameters are mutually dependent and are computed in an iterative way with the updating expressions given below. In these expressions, the superscript i will denote the iteration step and, for clarity, the superscript $(i-1)$, which indicates that the values of variables are that of the previous iteration, will be omitted (variables without superscript are those at the previous iteration). For the same reason, the subscript n will be omitted in the contrast source updating expressions.

- Concerning the contrast sources, we obtain

$$\begin{aligned}
\tilde{\mathbf{m}}^i_w &= \tilde{\mathbf{m}}_w + \tilde{\mathbf{V}}^i_w[\overline{\gamma^{-2}_\epsilon}\mathbf{G}^{o\dagger}(\mathbf{E}^{\mathrm{sc}} - \mathbf{G}^o\tilde{\mathbf{m}}_w)\\
&+ \overline{\gamma^{-2}_\xi}(\mathbf{I} - \mathbf{G}^{c\dagger}\tilde{\mathbf{m}}^\dagger_\chi)(\tilde{\mathbf{M}}_\chi(\mathbf{E}^{\mathrm{inc}} + \mathbf{G}^c\tilde{\mathbf{m}}_w) - \tilde{\mathbf{m}}_w)\\
&+ \overline{\gamma^{-2}_\xi}\tilde{\mathbf{V}}_\chi(\mathbf{E}^{\mathrm{inc}} + \mathbf{G}^c\tilde{\mathbf{m}}_w)],\\
\tilde{\mathbf{V}}^i_w &= [\mathbf{Diag}(\overline{\gamma^{-2}_\epsilon}\Gamma^o + \overline{\gamma^{-2}_\xi}\,\overline{\Gamma^c})]^{-1},
\end{aligned} \tag{20}$$

where the overbar denotes the expectation of the variable with respect to q (i.e., $\overline{u} = \mathbb{E}(u)_q$) and superscript $\dagger$ indicates the conjugate transpose. In the above expression, $\tilde{\mathbf{M}}_\chi$ and $\tilde{\mathbf{V}}_\chi$ are diagonal matrices built up from the components of the vectors $\tilde{\mathbf{m}}_\chi$ and $\tilde{\mathbf{v}}_\chi$ ($\tilde{\mathbf{m}}_\chi = \{\tilde{m}_{\chi(\mathbf{r})}\}, \tilde{\mathbf{v}}_\chi = \{\tilde{v}_{\chi(\mathbf{r})}\}, \mathbf{r}\in\mathcal{D}$) that represent the means and variances of the cell contrasts, respectively, and Γ^o and $\overline{\Gamma^c}$ are given by

$$\begin{aligned}
\Gamma^o(\mathbf{r}) &= \sum_{\mathbf{r}'}|G^o(\mathbf{r}',\mathbf{r})|^2,\\
\overline{\Gamma^c}(\mathbf{r}) &= 1 - 2\Re e[G^c(\mathbf{r},\mathbf{r})\tilde{m}_\chi(\mathbf{r})]\\
&+ [\tilde{m}^2_\chi(\mathbf{r}) + \tilde{v}_\chi(\mathbf{r})]\sum_{\mathbf{r}'}|G^c(\mathbf{r}',\mathbf{r})|^2.
\end{aligned} \tag{21}$$

- Concerning the contrast χ, the updates read

$$\tilde{\mathbf{m}}_\chi^i = \tilde{\mathbf{V}}_\chi^i \left(\sum_k \overline{\gamma_k^{-2}}\, \tilde{\zeta}_k \tilde{\mu}_k + \sum_n \overline{\gamma_{\xi_n}^{-2}}\, \overline{\mathbf{w}_n \mathbf{E}_n^*} \right),$$
$$\tilde{\mathbf{V}}_\chi^i = \left[\mathbf{Diag}\left(\sum_n \overline{\gamma_{\xi_n}^{-2}}\, \overline{\mathbf{E}_n^2} + \overline{\mathbf{V}_\chi^{-1}} \right) \right]^{-1}, \quad (22)$$

where $*$ denotes the complex conjugate and $\overline{\mathbf{w}_n \mathbf{E}_n^*}$ is such that

$$\overline{w_n E_n^*}(\mathbf{r}) = E_n^{\mathrm{inc}*}(\mathbf{r}) \tilde{m}_{w_n}(\mathbf{r}) + G_n^{c*}(\mathbf{r},\mathbf{r}) \tilde{v}_{w_n}(\mathbf{r}) + \tilde{m}_{w_n}(\mathbf{r}) \sum_{\mathbf{r}'} G_n^{c*}(\mathbf{r},\mathbf{r}') \tilde{m}_{w_n}^*(\mathbf{r}'). \quad (23)$$

In equation 22, $\overline{\mathbf{V}_\chi^{-1}}$ and $\overline{\mathbf{E}_n^2}$ are diagonal matrices of which elements read

$$\overline{V_\chi^{-1}}(\mathbf{r},\mathbf{r}) = \sum_k \tilde{\zeta}_k(\mathbf{r}) \overline{\gamma_k^{-2}},$$
$$\overline{E_n^2}(\mathbf{r},\mathbf{r}) = |E_n^{\mathrm{inc}}(\mathbf{r})|^2 + 2\Re e[E_n^{\mathrm{inc}*}(\mathbf{r}) G_n^c(\mathbf{r},\mathbf{r}) \tilde{m}_{w_n}(\mathbf{r})] + \left| \sum_{\mathbf{r}'} G_n^c(\mathbf{r},\mathbf{r}') \tilde{m}_{w_n}(\mathbf{r}) \right|^2 + \sum_{\mathbf{r}'} |G_n^c(\mathbf{r},\mathbf{r}')|^2 \tilde{v}_{w_n}(\mathbf{r}). \quad (24)$$

- The parameter of the hidden field distribution is

$$\tilde{\zeta}_k^i(\mathbf{r}) = \exp\left(-\frac{1}{2} \left\{ \Psi(\tilde{\eta}_k) + \log(\tilde{\phi}_k) - \Upsilon \sum_{\mathbf{r}' \in \nu(\mathbf{r})} \tilde{\zeta}_k(\mathbf{r}') + \overline{\gamma_k^{-2}} [(\tilde{m}_{\boldsymbol{\chi}}(\mathbf{r}) - \tilde{\mu}_k)^2 + \tilde{\tau}_k + \tilde{v}_\chi(\mathbf{r})] \right\} \right), \quad (25)$$

where Ψ stands for the digamma function.

- For each frequency and source position, the parameters of the observation and coupling noise variances are

$$\tilde{\phi}_\epsilon^i = \phi_\epsilon + \frac{N_S}{2}, \quad \tilde{\phi}_\xi^i = \phi_\xi + \frac{N_D}{2},$$
$$\tilde{\eta}_\epsilon^i = \eta_\epsilon + \frac{1}{2}[\|\mathbf{E}^{\mathrm{sc}}\|_{\mathcal{S}}^2 + \|\mathbf{G}^o \tilde{\mathbf{m}}_w\|_{\mathcal{S}}^2 - 2\Re e(\mathbf{E}^{\mathrm{sc}\dagger} \mathbf{G}^o \tilde{\mathbf{m}}_w) + \|\mathbf{G}_o^2 \tilde{\mathbf{v}}_w\|_{L^1}],$$
$$\tilde{\eta}_\xi^i = \eta_\xi + \frac{1}{2}[\|\tilde{\mathbf{m}}_w\|_{\mathcal{D}}^2 + \|\tilde{\mathbf{V}}_w\|_{L^1} + \|(\tilde{\mathbf{M}}_\chi^\dagger \tilde{\mathbf{M}}_\chi + \tilde{\mathbf{V}}_\chi) \overline{E^2}\|_{L^1} - 2\Re e(\tilde{\mathbf{m}}_\chi^\dagger \overline{\mathbf{w}\mathbf{E}^*})], \quad (26)$$

where $\|.\|_{L^1}$ represents the L^1 norm and the elements of $\mathbf{G}_o^2$ are the squared elements of $\mathbf{G}^o$.

- The parameters that concern the variances of the classes are

$$\tilde{\phi}_k^i = \phi_0 + \frac{1}{2} \sum_{\mathbf{r}} \tilde{\zeta}_k(\mathbf{r}),$$
$$\tilde{\eta}_k^i = \eta_0 + \frac{1}{2} \sum_{\mathbf{r}} \tilde{\zeta}_k(\mathbf{r}) (|\tilde{m}_{\boldsymbol{\chi}}(\mathbf{r})|^2 + \tilde{v}_{\boldsymbol{\chi}}(\mathbf{r}) + \tilde{m}_k^2 + \tilde{\tau}_k^2). \quad (27)$$

- Finally, the means of the classes involve the following parameters:

$$\tilde{\tau}_k^i = \left[\tau_0^{-1} + \overline{\gamma_k^{-2}} \sum_{\mathbf{r}} \tilde{\zeta}_k(\mathbf{r}) \right]^{-1},$$
$$\tilde{\mu}_k^i = \tilde{\tau}_k \left[\frac{\mu_0}{\tau_0} + \overline{\gamma_k^{-2}} \sum_{\mathbf{r}} \tilde{\zeta}_k(\mathbf{r}) \tilde{m}_{\boldsymbol{\chi}}(\mathbf{r}) \right]. \quad (28)$$

The reconstruction algorithm

In the algorithm, the tilted parameters are updated iteratively following formulas given in the previous section until convergence is reached. The latter is evaluated empirically by looking at the evolution of the contrast and hyperparameters through the iterative process. Finally, the VBA algorithm can be summarized as follows:

VBA algorithm
Set initial estimates: $\chi^{(0)}, \mathbf{w}^{(0)}, \mathbf{h}^{(0)}$ and $\boldsymbol{\psi}^{(0)}$,
repeat

determine $q(\mathbf{h})$: update $\tilde{\zeta}_k$ using equation 25,
determine $q(\gamma_\epsilon^2)$ and $q(\gamma_\xi^2)$: update $\tilde{\phi}_\epsilon$, $\tilde{\eta}_\epsilon$, $\tilde{\phi}_\xi$ and $\tilde{\eta}_\xi$ using equations 26,
determine $q(\gamma_k^2)$: update $\tilde{\phi}_k$ and $\tilde{\eta}_k$ using equations 27,
determine $q(m_k)$: update $\tilde{\tau}_k$ and $\tilde{\mu}_k$ using equations 28,
determine $q(\mathbf{w})$: update $\tilde{\mathbf{m}}_w$ and $\tilde{\boldsymbol{V}}_w$ using equations 20,
determine $q(\chi)$: update $\tilde{\mathbf{m}}_{\boldsymbol{\chi}}$ and $\tilde{\boldsymbol{V}}_{\boldsymbol{\chi}}$ using equations 22,

until convergence.

APPLICATION AND RESULTS

A synthetic crosswell experiment

Let us consider a simple synthetic crosswell experiment in which the body is made of two 32 m sided cubic blocks, of which respective resistivities are 60 Ωm (resistive inhomogeneity) and 2 Ωm (conductive inhomogeneity), disposed as indicated in Figure 2a. This body is sought in a 112 m sided cubic test domain centered at (0, 0, 1413 m) and embedded in a 11-layer stratified underground (Figure 2b; Ogaya et al., 2014). The test domain is subdivided into $14 \times 14 \times 14$ cubic cells and, hence, the total number of conductivity contrast unknowns

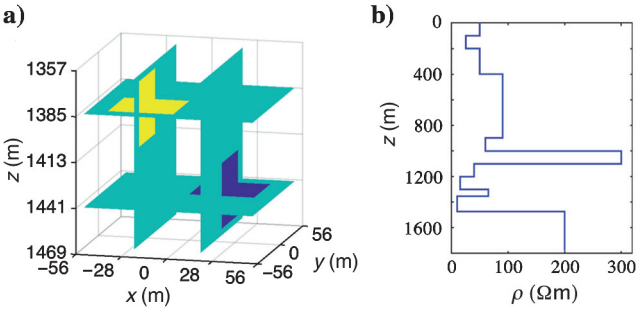

Figure 2. (a) The body is made of two 32 m sided cubic inhomogeneities: a resistive one (yellow, $\rho = 60$ Ωm) and a conductive one (blue, $\rho = 2$ Ωm), centered at ($x = -20$ m, $y = -20$ m, $z = 1385$ m) and ($x = 20$ m, $y = 20$ m, $z = 1441$ m), respectively, and located in a 112 m thick layer (with resistivity $\rho = 10$ Ωm) of (b) a stratified underground whose resistivity profile is taken from Ogaya et al. (2014).

DOI:10.1190/geo2016-0682.1

is equal to 2744. Four boreholes are located around this test domain at horizontal positions (x [m], y [m]) = (−65, −65), (−65, 65), (65, −65), and (65, 65). In each borehole, six sources (vertical electric dipoles) are located every 30 m, ranging from 1333 to 1483 m, whereas the vertical component of the electric field is measured at nine locations, every 25 m from 1313 to 1513 m, for six different frequencies (i.e., 16, 64, 256, 1024, 4096, and 16,384 Hz). This leads to the collection of 5184 scattered field data. Before inversion, the data corresponding to each frequency are corrupted with an additive white Gaussian noise with zero mean and variance γ_f^2, where γ_f is arbitrarily set to 2% of the maximum signal received at the given frequency.

Reconstructions

The VBA method requires an initialization for the contrast $\boldsymbol{\chi}^{(0)}$, the induced sources $\mathbf{w}^{(0)}$, the hidden field $\mathbf{h}^{(0)}$, and the hyperparameters $\boldsymbol{\psi}^{(0)}$. The initial values of the unknowns $\mathbf{w}^{(0)}$ and $\boldsymbol{\chi}^{(0)}$ are obtained either by back propagating the scattered field data from the measurement domain $\mathcal{S}$ onto the test domain $\mathcal{D}$ or as a result of a few CSI iteration steps. Initial hyperparameters $\boldsymbol{\psi}^{(0)}$ are set by means of empirical estimators. Given the initial contrast $\boldsymbol{\chi}^{(0)}$ and the number of classes N_k, the initial segmentation $\mathbf{h}^{(0)}$ is obtained by k-means clustering. Concerning the number of classes, when unknown, it can be initialized at a high level. In this case, previous works have highlighted an interesting behavior of the algorithm (Ayasso et al., 2012; Gharsalli et al., 2014); i.e., the number of classes identified during the iterative process converges to the actual one via two processes: If the number of cells in a given class decreases to a low threshold value, the class ends up vanishing or, if the means of two classes come very close to each other, these classes merge. This behavior is highlighted in Figure 3a that displays the evolution of the number of cells in each class versus the iteration step. Indeed, here, the number of classes is supposed to be unknown and initialized at $N_k = 5$, whereas the actual one is three (the background layer and the resistive and conductive anomalies), and it can be observed in this figure that the two material classes in excess quickly vanish in the first 20 iterations.

Figure 3b and 3c display the evolution of class means and variances, respectively. The evolution of these hyperparameters is useful to assess the convergence of the VBA algorithm, together with that of the observation and coupling error variances. In Figure 3b and 3c, it can be observed that the mean resistivities of classes 1 and 5 (corresponding to the resistive and conductive heterogeneities, respectively) tend to slowly increase and decrease toward the good values and that the variances of these classes slowly decrease, which leads to more homogeneous materials. In this figure, the evolution of the various parameters is displayed with a logarithmic iteration scale, which highlights their behavior in the first 50 iterations but interferes with the perception of convergence. Figure 4 displays the evolution of the observation and coupling errors ($\sum_n \|\mathbf{E}_n^{\text{sc}} - \mathbf{G}_n^o \mathbf{w}_n\|_{\mathcal{S}}^2$ and $\sum_n \|\mathbf{w}_n - \boldsymbol{\chi}\mathbf{E}_n^{\text{inc}} - \boldsymbol{\chi}G_n^c \mathbf{w}_n\|_{\mathcal{D}}^2$, respectively) during the inversion process. Both errors are decaying of several orders of magnitude, much faster during the first 50 iterations than latter. It can be noted that, when a single frequency is considered (i.e., 256 Hz), convergence is deemed to be reached after 1000 iterations as the root-mean-square (rms) error is close to 1 ($\text{rms error} = \sqrt{\sum_n \|\mathbf{E}_n^{\text{sc}} - \mathbf{G}_n^o \mathbf{w}_n\|_{\mathcal{S}}^2 / \sum_n N_S} = 1.14$), and the various parameters of the model do not evolve anymore after that, but this is no more true when the above defined six frequencies are accounted for, as in Figures 3 and 4. In that case, the parameters of classes 1 and 5 are still evolving after that, but, due to competition between the different frequencies, convergence is very slow and 1000 iterations more would not have significantly changed the reconstructed model. This is the reason why, to compare with the single-

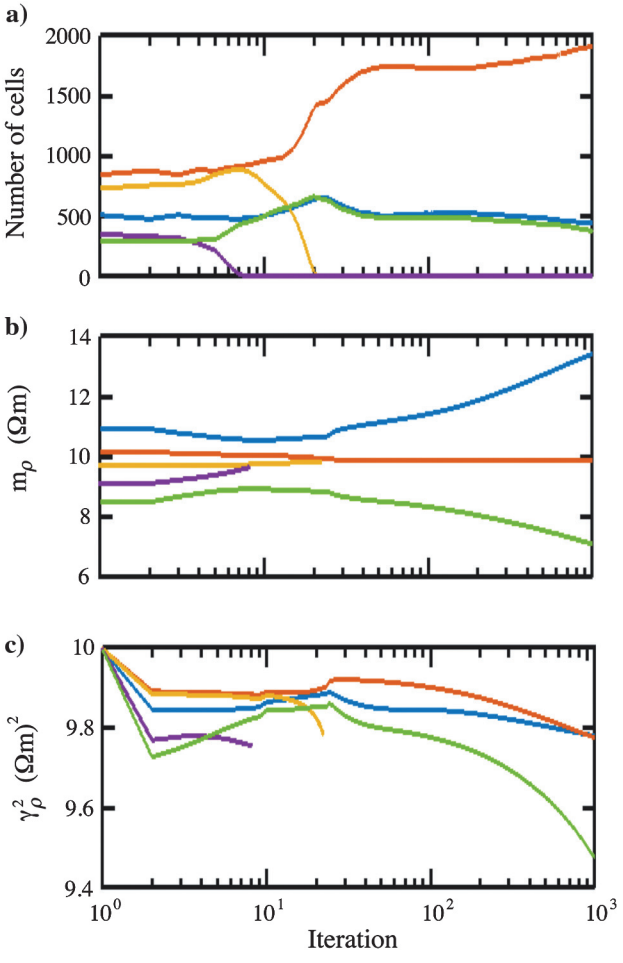

Figure 3. Evolution of the class parameters for the multifrequency VBA inversion: (a) number of cells in each class, (b) class means and (c) class variances. Class 1 (blue line), class 2 (red line), and class 5 (green line) correspond to the resistive anomaly, to the background layer and to the conductive anomaly, respectively.

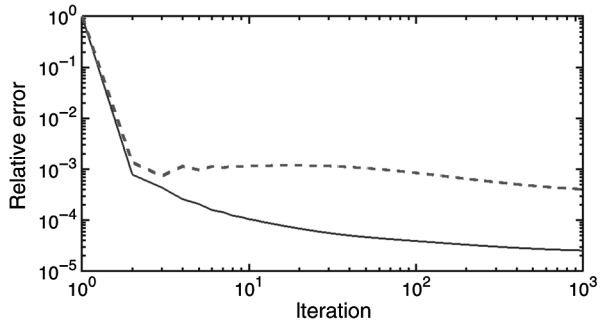

Figure 4. Evolution of the observation and coupling errors versus the iteration step for the multifrequency VBA inversion: (full line) observation error, (dashed line) coupling error. Both errors are normalized with respect to their value at the first iteration.

frequency case, the process is stopped after 1000 iterations, although the rms error is still at a high level (rms error = 1.65) due to large misfits at the higher frequencies (4096 Hz and, more critically, 16 kHz).

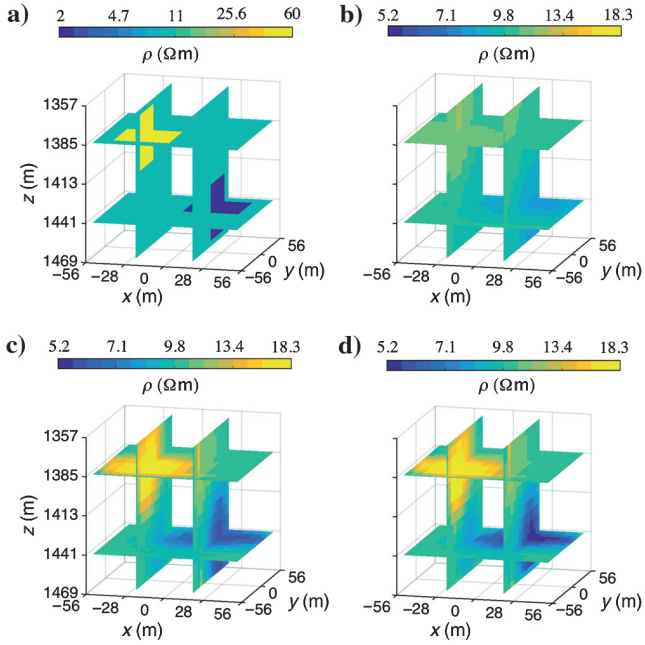

Figure 5. Resistivity maps: (a) the actual resistivity is compared with that retrieved by (b) CSI with six frequencies, (c) VBA with one frequency and (d) VBA with six frequencies. It can be noted that the color scale of the retrieved profiles is different from that of the actual one.

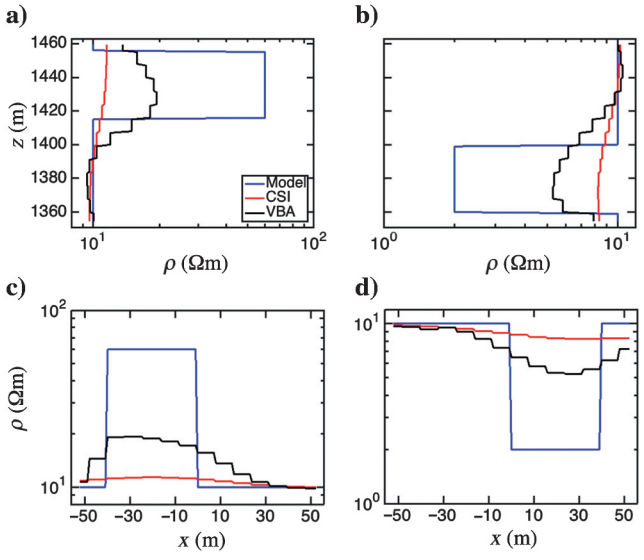

Figure 6. The actual resistivity profile (blue line) compared with that retrieved in the multifrequency case by means of CSI (red line) and VBA (black line) along (a and b) vertical lines passing at (a) ($x = -20$ m, $y = -20$ m) and (b) ($x = 20$ m, $y = 20$ m) and (c and d) horizontal lines passing at (c) ($y = -20$ m, $z = 1385$ m) and (d) ($y = 20$ m, $z = 1441$ m). On the left, the profiles pass through the resistive anomaly, whereas on the right they pass through the conductive one.

Figure 5 compares the actual resistivity map to that obtained by means of CSI and VBA. Contrast source inversion is applied to multifrequency data and stopped after 300 iterations, whereas VBA is applied to multifrequency and single-frequency (256 Hz) data. Due to a priori information introduced in the inversion algorithm, the quality of the reconstruction is significantly improved with VBA. In particular, the algorithm performs better than CSI in retrieving homogeneous regions corresponding to the two inhomogeneities, with resistivity values much closer to the actual ones, as it can be observed in Figure 6 which depicts the resistivity profiles reconstructed along vertical and horizontal lines crossing the two body blocks. In this figure, it can be observed that the maximal resistivity contrast retrieved by VBA reaches 18% and 62% of the actual contrasts for the resistive and conductive inhomogeneities, respectively, which represents a very good reconstruction compared with the 4% (resistive anomaly) and 27% (conductive anomaly) of the actual resistivity contrast reached by CSI. Of course, accounting for additional constraints in the functional to be minimized, such as a total variation term (Abubakar and van den Berg, 2002), would have led CSI to retrieve more compact anomalies and, thus, to yield re-

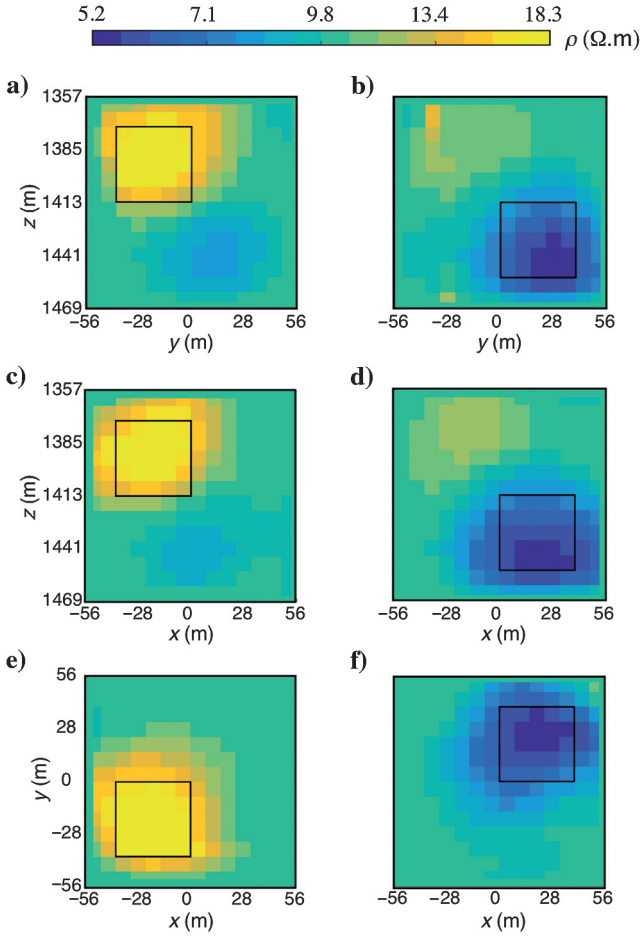

Figure 7. Two-dimensional cross-sections of the resistivity map obtained by means of VBA with six frequencies passing through (a, c, and e) the resistive and (b, d, and f) the conductive anomalies: (a and b) y-z cross sections at (a) $x = -20$ m and (b) $x = 20$ m, (c and d) x-z cross sections at (c) $y = -20$ m and (d) $y = 20$ m and (e and f) x-y cross-sections at (e) $z = 1384$ m and (f) $z = 1441$ m. The contours of the actual anomalies are displayed in black lines.

sults closer to that of VBA. The results obtained by means of the six-frequency VBA inversion concerning the shape and location of the retrieved body are detailed in Figure 7 which displays cross sections of the resistivity map in six vertical and horizontal planes passing through the centers of the actual anomalies. The size and location of the retrieved resistive anomaly are in very good agreement with the actual ones. As for the conductive anomaly, its location is well-retrieved, but its contours are not well described. Figure 8 displays cross sections of the contrast variance map in the same planes as Figure 7: The contrast variance quantifies the uncertainty on the retrieved contrast, the yellow cells being those whose contrast values are the most uncertain.

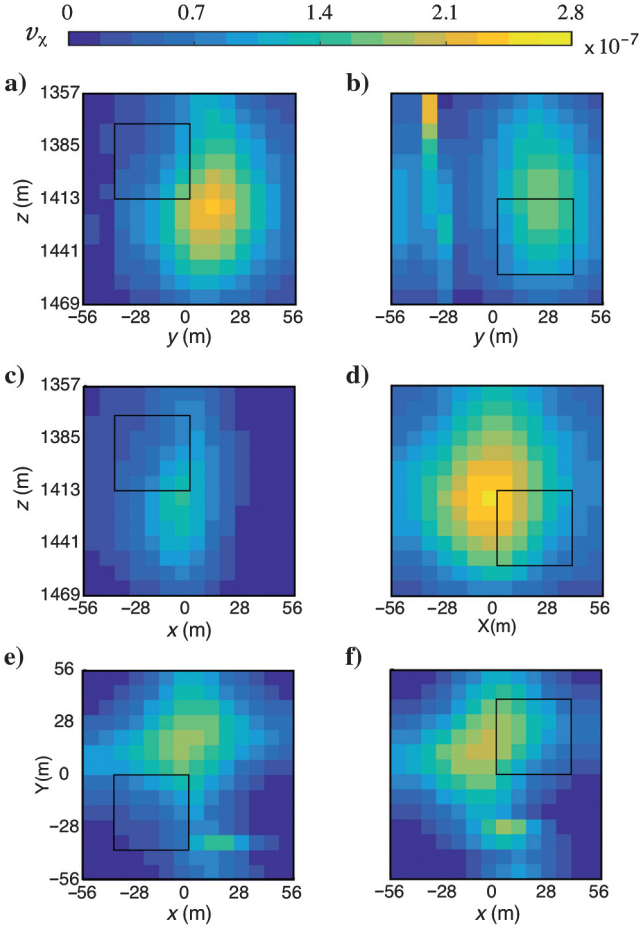

Figure 8. Two-dimensional cross sections of the contrast variance map corresponding to the resistivity maps displayed in Figure 7.

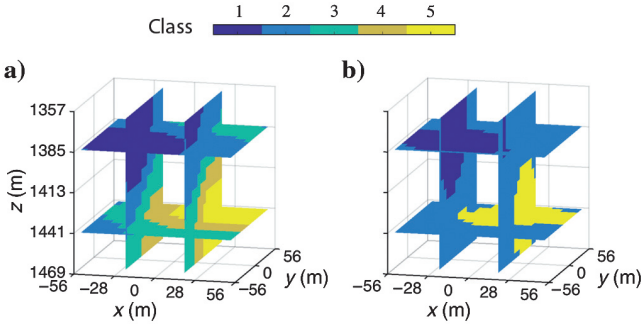

Figure 9. Segmentation of the resistivity model obtained with the multifrequency VBA inversion: (a) the initial segmentation into five classes obtained by k-means clustering and (b) the final segmentation in which only three classes remain, class 1 (dark blue, the resistive anomaly), class 2 (blue, the background), and class 5 (yellow, the conductive anomaly).

The evolution of the material distribution is depicted in Figure 9 that displays the initial (derived from k-means clustering) and final segmentations. In the final segmentation, resistive and conductive anomalies appear at the right locations. Nevertheless, they are not as compact as the actual anomalies. It should be mentioned that size and homogeneity of the regions that are obtained at the end of the iterative process can be controlled by means of the Potts parameter Υ (see equation 15): The smaller Υ is, the smaller the homogeneous regions are (Ayasso, 2010). Herein, this parameter has been set to a value close to, but smaller than, a critical value $\Upsilon_c = \log(1 + \sqrt{N_k})$ (Beffara and Duminil-Copin, 2012) so that small anomalies, that could be present in a situation on the ground, can be recovered whereas the number of homogeneous regions in the final image remains reasonably low.

At a computational point of view, VBA requires more memory than CSI due to the additional variables (hidden field, hyperparameters). It also converges slower than CSI, but VBA iterations are faster than that of CSI. In the multifrequency case considered herein, one iteration takes 49.3 s with VBA against 103.2 s with CSI on a laptop with a 2.1 GHz processor. In this case, the total time needed by VBA to reach convergence is about 1.5 times that needed by CSI, but the convergence of VBA can be speeded-up by means of a gradient-like variational Bayesian method (Fraysse and Rodet, 2014) that is under investigation and has already shown its effectiveness compared with the classical VBA in other applications.

In Figure 5, it can be observed that using a single frequency or the whole frequency set leads to almost similar results. This can be explained by information redundancy (Bucci et al., 2001) of the experimental configuration considered here, in which data are collected for numerous sources and receivers disposed all around the body. On the contrary, in realistic situations, data would be collected in various surface-to-surface or well-to-surface measurement configurations, possibly by using LEMAM arrays (Bourgeois and Girard, 2010), and, with such aspect limited data, multifrequency inversion would be essential to get a sufficient sensitivity to the vertical location of anomalies.

Finally, in the synthetic experiment considered herein, for the sake of simplicity the sought body consists of two distinct heterogeneities embedded in the same layer, but the case of numerous heterogeneities dispersed in several layers could also be considered.

CONCLUSION

This paper deals with a Bayesian method applied to the inversion of 3D CSEM geophysical data. The goal is to retrieve a map of resistivity of an unknown body embedded in a layered underground from measurements of the scattered electric field that results from its interaction with a known interrogating wave. This constitutes an inverse scattering problem that is known to be ill-posed, so that needs to be regularized. Regularization is generally performed by introducing a priori information on the expected solution. Deterministic inversion methods, such as CSI, introduce a priori information by adding a penalization term in the cost functional to be

minimized. The choice of a priori that can be introduced in this way is limited, and this often leads to suboptimal solutions. Herein, a priori information that we would like to account for consists of the fact that the sought body is made of a finite number of different materials distributed in compact homogeneous regions and the Bayesian estimation framework allows us to easily introduce this prior knowledge by means of a Gauss-Markov-Potts prior model of the sought resistivity contrast.

The VBA presented here seeks to estimate the joint posterior distribution of all the unknowns as a separable distribution that gives the best approximation of the true posterior law in the Kullback-Leibler sense. The solution is a set of parametric distributions, with mutual dependency between the different variables, which are sought in an iterative way. The VBA method is applied to a synthetic cross-well CSEM experiment and compared with the deterministic CSI method. It is shown to perform better that CSI with regard to the retrieved resistivity contrast values and inhomogeneity locations. In addition, VBA has the advantage of providing not only the resistivity model but also its segmentation in regions and the material class parameters (means and variances) in each of these regions. This additional information could be of great help in the interpretation of the results. Furthermore, VBA yields a much faster estimation of the unknown posterior laws than the traditional MCMC method based upon a stochastic sampling. On the other hand, compared with CSI, VBA shows a slower convergence, but its convergence can be speeded up by means of a gradient-like variational Bayesian method. This time savings would be crucial for processing large-scale problems that occur in 3D electromagnetic geophysical exploration that could require up to several hundred thousand grid cells, and it could be even more enhanced by parallelizing the computations in the forward and inverse schemes. In addition to speed up the computations, a parallelization based on a domain decomposition of the test domain would also allow us to deal with high memory requirements linked to the integral equation — moment method forward model.

The next step would be to apply the algorithm to real experimental data, if the latter can be collected. This would require further developments of the algorithm and, particularly, the study of its behavior when applied to CSEM inversion in aspect limited data configurations.

ACKNOWLEDGMENTS

The authors would like to thank G. Newman (Lawrence Berkeley National Laboratory) for allowing them to use his EM3DS forward modeling code, B. Bourgeois (BRGM) for fruitful discussions relative to CSEM methods, and the reviewers for their numerous and wise comments. This work was funded by the French National Research Agency through the project EM-Hontomin (ANR-11-SEED-0008-03).

REFERENCES

Abubakar, A., 2000, Three-dimensional nonlinear inversion of electrical conductivity: Ph.D. thesis, Delft University.

Abubakar, A., T. Habashy, V. Druskin, D. Alumbaugh, A. Zerelli, and L. Knizhnerman, 2006, Two-and-half-dimensional forward and inverse modeling for marine CSEM problems: 76th Annual International Meeting, SEG, Expanded Abstracts, 750–754.

Abubakar, A., T. Habashy, M. Li, and J. Liu, 2009, Inversion algorithms for large-scale geophysical electromagnetic measurements: Inverse Problems, **25**, 123012, doi: 10.1088/0266-5611/25/12/123012.

Abubakar, A., and P. M. van den Berg, 1998, Three-dimensional nonlinear inversion in cross-well electrode logging: Radio Science, **33**, 989–1004, doi: 10.1029/98RS00975.

Abubakar, A., and P. M. van den Berg, 2000, Three-dimensional inverse scattering applied to cross-well induction sensors: IEEE Transactions on Geoscience and Remote Sensing, **38**, 1669–1681, doi: 10.1109/36.851966.

Abubakar, A., and P. M. van den Berg, 2002, A total variation enhanced contrast source inversion method for three-dimensional profile reconstruction: European Congress on Computational Methods in Applied Sciences and Engineering (ECCOMAS 2000), Proceedings, 1–19.

Ayasso, H., 2010, Une approche bayésienne de l'inversion. Application à l'imagerie de diffraction dans les domaines micro-onde et optique: Ph.D. thesis, Université Paris sud 11.

Ayasso, H., B. Duchêne, and A. Mohammad-Djafari, 2012, Optical diffraction tomography within a variational Bayesian framework: Inverse Problems in Science and Engineering, **20**, 59–73, doi: 10.1080/17415977.2011.624620.

Barrière, P. A., J. Idier, Y. Goussard, and J. J. Laurin, 2007, 3-term optimization criterion for faster inversion in microwave tomography: 4th IEEE International Symposium on Biomedical Imaging: From Nano to Macro, Proceedings, 225–228.

Beffara, V., and H. Duminil-Copin, 2012, The self-dual point of the two-dimensional random-cluster model is critical for $q \geq 1$: Probability Theory and Related Fields, **153**, 511–542, doi: 10.1007/s00440-011-0353-8.

Bernardo, J. M., and A. F. M. Smith, 2008, Bayesian theory: John Wiley & Sons Inc.

Bourgeois, B., and J. Girard, 2010, First modeling results of the EM response of a CO2 storage in the Paris basin: Oil & Gas Science and Technology– Rev. IFP, **65**, 597–614, doi: 10.2516/ogst/2009076.

Buland, A., and O. Kolbjørnsen, 2012, Bayesian inversion of CSEM and magnetotelluric data: Geophysics, **77**, no. 1, E33–E42, doi: 10.1190/geo2010-0298.1.

Bucci, O. M., L. Crocco, T. Isernia, and V. Pascazio, 2001, Subsurface inverse scattering problems: Quantifying, qualifying, and achieving the available information: IEEE Transactions on Geoscience and Remote Sensing, **39**, 2527–2538, doi: 10.1109/36.964991.

Charbonnier, P., L. Blanc-Féraud, G. Aubert, and M. Barlaud, 1997, Deterministic edge-preserving regularization in computed imaging: IEEE Transactions on Image Processing, **6**, 298–311, doi: 10.1109/83.551699.

Chen, J., G. Hoversten, D. Vasco, Y. Rubin, and Z. Hou, 2007, A Bayesian model for gas saturation estimation using marine seismic AVA and CSEM data: Geophysics, **72**, no. 2, WA85–WA95, doi: 10.1190/1.2435082.

Chew, W., 1995, Waves and fields in inhomogeneous media: IEEE Press.

Colton, D., and R. Kress, 1992, Inverse acoustic and electromagnetic scattering theory: Springer.doi: 10.1007/978-3-662-02835-3.

Commer, M., and G. A. Newman, 2009, Three-dimensional controlled-source electromagnetic and magnetotelluric joint inversion: Geophysical Journal International, **178**, 1305–1316, doi: 10.1111/j.1365-246X.2009.04216.x.

Constable, S., and C. J. Weiss, 2006, Mapping thin resistors and hydrocarbons with marine EM methods: Insights from 1D modeling: Geophysics, **71**, no. 2, G43–G51, doi: 10.1190/1.2187748.

Dorn, O., E. Miller, and C. Rappaport, 2000, A shape reconstruction method for electromagnetic tomography using adjoint fields and level sets: Inverse Problems, **16**, 1119–1156, doi: 10.1088/0266-5611/16/5/303.

Egbert, G. D., and A. Kelbert, 2012, Computational recipes for electromagnetic inverse problems: Geophysical Journal International, **189**, 251–267, doi: 10.1111/j.1365-246X.2011.05347.x.

Fraysse, A., and T. Rodet, 2014, A measure-theoretic variational Bayesian algorithm for large dimensional problems: SIAM Journal on Imaging Sciences, **7**, 2591–2622, doi: 10.1137/140966575.

Gao, G., 2005, Simulation of borehole electromagnetic measurements in dipping and anisotropic rock formations and inversion of array induction data: Ph.D. thesis, University of Texas.

Gehrmann, R. A. S., J. Dettmer, K. Schwalenberg, M. Engels, S. E. Dosso, and A. Özmaral, 2015, Trans-dimensional Bayesian inversion of controlled-source electromagnetic data in the German North Sea: Geophysical Prospecting, **63**, 1314–1333, doi: 10.1111/1365-2478.12308.

Gharsalli, L., H. Ayasso, B. Duchêne, and A. Mohammad-Djafari, 2014, Inverse scattering in a Bayesian framework: Application to microwave imaging for breast cancer detection: Inverse Problems, **30**, 114011, doi: 10.1088/0266-5611/30/11/114011.

Goreinov, S. A., D. V. Savostyanov, and E. E. Tyrtyshnikov, 2009, Tensor and Toeplitz structures applied to direct and inverse 3D electromagnetic problems: 26th Progress In Electromagnetic Research Symposium, Proceedings, 1896–1900.

Gribenko, A., and M. Zhdanov, 2007, Rigorous 3D inversion of marine CSEM data based on the integral equation method: Geophysics, **72**, no. 2, WA73–WA84, doi: 10.1190/1.2435712.

Gunning, J., M. Glinsky, and J. Hedditch, 2010, Resolution and uncertainty in 1D CSEM inversion: A Bayesian approach and open-source implementation: Geophysics, **75**, no. 6, F151–F171, doi: 10.1190/1.3496902.

Habashi, T., R. Groom, and B. Spies, 1993, Beyond the Born and Rytov approximations: Journal of Geophysical Research-Solid Earth, **98**, 1759–1775, doi: 10.1029/92JB02324.
Hinton, G. E., and D. Van Camp, 1993, Keeping the neural networks simple by minimizing the description length of the weights: Sixth Annual Conference on Computational Learning Theory (COLT'93), Proceedings, 5–13.
Hokstad, K., and T. Røsten, 2007, On the relationships between depth migration of controlled-source electromagnetic and seismic data: The Leading Edge, **26**, 342–347, doi: 10.1190/1.2715061.
Hunziker, J., J. Thorbecke, and E. Slob, 2014, Probing the solution space of an EM inversion problem with a genetic algorithm: 84th Annual International Meeting, SEG, Expanded Abstracts, 833–837.
Kleinman, R. E., and P. M. van den Berg, 1992, A modified gradient method for two-dimensional problems in tomography: Journal of Computational and Applied Mathematics, **42**, 17–35, doi: 10.1016/0377-0427(92)90160-Y.
Kullback, S., and R. A. Leibler, 1951, On information and sufficiency: The Annals of Mathematical Statistics, **22**, 79–86.doi: 10.1214/aoms/1177729694.
Lesselier, D., and B. Duchêne, 1991, Buried 2-D penetrable objects illuminated by line-sources: FFT-based iterative computations of the anomalous field, *in* T. K. Sarkar, ed., Application of conjugate gradient methods to electromagnetics and signal analysis, PIER: Elsevier **5**, 351–389.
Li, F., Q. H. Liu, and L.-P. Song, 2004, Three-dimensional reconstruction of objects buried in layered media using Born and distorted Born iterative methods: IEEE Geoscience and Remote Sensing Letters, **1**, 107–111, doi: 10.1109/LGRS.2004.826562.
Li, M., A. Abubakar, J. Liu, G. Pan, and T. M. Habashy, 2011, A compressed implicit Jacobian scheme for 3D electromagnetic data inversion: Geophysics, **76**, no. 3, F173–F183, doi: 10.1190/1.3569482.
Miller, E. L., M. Kilmer, and C. Rappaport, 2000, A new shape-based method for object localization and characterization from scattered field data: IEEE Transactions on Geoscience and Remote Sensing, **38**, 1682–1696, doi: 10.1109/36.851967.
Minsley, B., 2011, A trans-dimensional Bayesian Markov chain Monte-Carlo algorithm for model assessment using frequency-domain electromagnetic data: Geophysical Journal International, **187**, 252–272, doi: 10.1111/j.1365-246X.2011.05165.x.
Mohammad-Djafari, A., 2008, Gauss-Markov-Potts prior for images in computer tomography resulting to joint optimal reconstruction and segmentation: International Journal of Tomography and Statistics, **11**, 76–92.
Mohammad-Djafari, A., 2015, Entropy, information theory, information geometry and Bayesian inference in data, signal and image processing and inverse problems: Entropy, **17**, 3989–4027, doi: 10.3390/e17063989.
Mosegaard, K., and M. Sambridge, 2002, Monte Carlo analysis of inverse problems: Inverse Problems, **18**, R29–R54, doi: 10.1088/0266-5611/18/3/201.
Newman, G. A., and G. W. Hohmann, 1988, Transient electromagnetic responses of high-contrast prisms in a layered earth: Geophysics, **53**, 691–706, doi: 10.1190/1.1442503.
Newman, G. A., G. W. Hohmann, and W. L. Anderson, 1986, Transient electromagnetic response of a three-dimensional body in a layered earth: Geophysics, **51**, 1608–1627, doi: 10.1190/1.1442212.
Ogaya, X., P. Queralt, J. Ledo, Á. Marcuello, and A. G. Jones, 2014, Geoelectrical baseline model of the subsurface of the Hontomín site (Spain) for CO_2geological storage in a deep saline aquifer: A 3D magnetotelluric characterisation: International Journal of Greenhouse Gas Control, **27**, 120–138, doi: 10.1016/j.ijggc.2014.04.030.
Plessix, R.-E., and W. A. Mulder, 2008, Resistivity imaging with controlled-source electromagnetic data: Depth and data weighting: Inverse Problems, **24**, 034012, doi: 10.1088/0266-5611/24/3/034012.
Portniaguine, O., and M. S. Zhdanov, 1999, Focusing geophysical inversion images: Geophysics, **64**, 874–887, doi: 10.1190/1.1444596.
Ray, A., D. L. Alumbaugh, G. N. Hoversten, and K. Key, 2013, Robust and accelerated Bayesian inversion of marine controlled-source electromagnetic data using parallel tempering: Geophysics, **78**, no. 6, E271–E280, doi: 10.1190/geo2013-0128.1.
Ray, A., and K. Key, 2012, Bayesian inversion of marine CSEM data with a trans-dimensional self parametrizing algorithm: Geophysical Journal International, **191**, 1135–1151.
Ray, A., K. Key, T. Bodin, D. Myer, and S. Constable, 2014, Bayesian inversion of marine CSEM data from the Scarborough gas field using a transdimensional 2-D parametrization: Geophysical Journal International, **199**, 1847–1860, doi: 10.1093/gji/ggu370.
Robert, C., and G. Casella, 2000, Monte-Carlo statistical methods: Springer.
Roth, F., and J. J. Zach, 2007, Inversion of marine CSEM data using up–down wavefield separation and simulated annealing: 77th Annual International Meeting, SEG, Expanded Abstracts, 524–528.
Rothman, D. H., 1986, Automatic estimation of large residual statics corrections: Geophysics, **51**, 332–346, doi: 10.1190/1.1442092.
Sen, M. K., and P. L. Stoffa, 1996, Bayesian inference, Gibbs' sampler and uncertainty estimation in geophysical inversion: Geophysical Prospecting, **44**, 313–350, doi: 10.1111/j.1365-2478.1996.tb00152.x.
Šmídl, V., and A. Quinn, 2006, The variational Bayes method in signal processing: Springer.
Tarantola, A., and B. Valette, 1982, Inverse problems = quest for information: Journal of Geophysics, **50**, 159–170.
Tikhonov, A. N., 1963, Solution of incorrectly formulated problems and the regularization method: Soviet Mathematics Doklady Journal, **4**, 1035–1038.
Trainor-Guitton, W., and G. Hoversten, 2011, Stochastic inversion for electromagnetic geophysics: Practical challenges and improving convergence efficiency: Geophysics, **76**, no. 6, F373–F386, doi: 10.1190/geo2010-0223.1.
van den Berg, P. M., and A. Abubakar, 2001, Contrast source inversion method: State of art: Progress In Electromagnetics Research, **34**, 189–218, doi: 10.2528/PIER01061103.
van den Berg, P. M., and R. E. Kleinman, 1997, A contrast source inversion method: Inverse Problems, **13**, 1607–1620, doi: 10.1088/0266-5611/13/6/013.
Vilamajó, E., B. Rondeleux, P. Queralt, A. Marcuello, and J. Ledo, 2015, A land controlled source electromagnetic experiment using a deep vertical electric dipole: Experimental settings, processing, and first data interpretation: Geophysical Prospecting, **63**, 1527–1540, doi: 10.1111/1365-2478.12331.
Wang, L., A. Mohammad-Djafari, N. Gac, and M. Dumitru, 2016, Computed tomography reconstruction based on a hierarchical model and variational Bayesian method: IEEE International Conference on Acoustics, Speech and Signal Processing (ICASSP), Proceedings, 883–887.
Wannamaker, P. E., G. W. Hohmann, and W. A. SanFilipo, 1984, Electromagnetic modeling of three-dimensional bodies in layered earths using integral equations: Geophysics, **49**, 60–74, doi: 10.1190/1.1441562.
Wiik, T., L. Løseth, B. Ursin, and K. Hokstad, 2011, TIV contrast source inversion of mCSEM data: Geophysics, **76**, no. 1, F65–F76, doi: 10.1190/1.3524270.
Xu, X. M., and Q. H. Liu, 2002, The BCGS-FFT method for electromagnetic scattering from inhomogeneous objects in a planarly layered medium: IEEE Antennas and Wireless Propagation Letters, **1**, 77–80, doi: 10.1109/LAWP.2002.802549.
Zhdanov, M., and S. Fang, 1996, 3D quasi-linear electromagnetic inversion: Radio Science, **31**, 741–754, doi: 10.1029/96RS00719.
Zhdanov, M. S., P. Traynin, and J. R. Booker, 1996, Underground imaging by frequency-domain electromagnetic migration: Geophysics, **61**, 666–682, doi: 10.1190/1.1443995.